DC dynamic pull-in predictions for a generalized clamped–clamped micro-beam based on a continuous model and bifurcation analysis

DC dynamic pull-in predictions for a generalized clamped–clamped micro-beam based on a continuous model and bifurcation analysis

Paul C-P Chao[1], C W Chiu[2] and Tsu-Hsien Liu[2]

[1] Associate Professor, Department of Electrical and Control Engineering, National Chiao Tung University, Hsinchu 300, Taiwan, Republic of China
[2] Graduate Students, Department of Electrical and Control Engineering, National Chiao Tung University, Hsinchu 300, Taiwan, Republic of China

E-mail: pchao@mail.nctu.edu.tw

Abstract
This study is devoted to providing precise predictions of the dc dynamic pull-in voltages of a clamped–clamped micro-beam based on a continuous model. A pull-in phenomenon occurs when the electrostatic force on the micro-beam exceeds the elastic restoring force exerted by beam deformation, leading to contact between the actuated beam and bottom electrode. DC dynamic pull-in means that an instantaneous application of the voltage (a step function such as voltage) is applied. To derive the pull-in voltage, a dynamic model in partial differential equations is established based on the equilibrium among beam flexibility, inertia, residual stress, squeeze film, distributed electrostatic forces and its electrical field fringing effects. The method of Galerkin decomposition is then employed to convert the established system equations into reduced discrete modal equations. Considering lower-order modes and approximating the beam deflection by a different order series, bifurcation based on phase portraits is conducted to derive static and dynamic pull-in voltages. It is found that the static pull-in phenomenon follows dynamic instabilities, and the dc dynamic pull-in voltage is around 91–92% of the static counterpart. However, the derived dynamic pull-in voltage is found to be dependent on the varied beam parameters, different from a fixed predicted value derived in past works, where only lumped models are assumed. Furthermore, accurate closed-form predictions are provided for non-narrow beams. The predictions are finally validated by finite element analysis and available experimental data.

(Some figures in this article are in colour only in the electronic version)

1. Introduction

Recent advances in the technology of micro-electro-mechanical systems (MEMS) have accelerated the design and application of micro-sensors and actuators based on electrostatic actuation, such as pressure sensors [1, 2], microphones [3, 4] and optical/RF switches [5–9] in varied structures. Electrostatic devices are, in fact, capacitors that are composed of one deformable electrode and another

fixed electrode (backplate). With the application of a cross voltage the flexible electrode deforms and then touches the fixed electrodes for different application objectives. Some applications, such as microphones [3, 4] or pressure sensors [1, 2], must be only operated within a safe range without pull-in occurrence, while others, such as optical/RF switches [5–9], need to tune the bias voltage across the pull-in back and forth to alternate switch on and off. In all the aforementioned applications, information on the critical bias voltage as the

pull-in occurs (so-called pull-in voltage) must be precisely computed before usage, and thus provided to designers for meeting the required device specifications.

There have been some research works devoted to predicting pull-in occurrence for a variety of electrostatic sensors and actuators [10]. In these studies, pull-in problems were initially predicted without considering the dynamics of the deformed electrode, deriving the so-called static pull-in condition. In later works, to reflect operation reality, the applied voltage is considered in varied fashions of dc voltage (step voltage input), ac voltage (harmonic-like voltage input) or combined ac/dc voltage to consider the dynamics of the deformed electrode for rendering more precise pull-in voltage predictions. Note that the present study is primarily devoted to the precise prediction of dc dynamic pull-in voltage with clear comparison with static counterparts to stress the necessity for dc dynamic pull-in voltage prediction.

For static pull-in, early works [11–13] assumed a 1D lumped model to approximate the behaviors of deformed beams/plates, with the aim to predict the static pull-in phenomenon. Recognizing that the inevitable error resulted from the approximation of the deformed plates/beams by the lumped model, some researches were conducted based on continuous models [14–25] or finite element models (FEM) [13, 18, 20, 26]. These works, which use continuous models, aim to obtain analytical predictions on the static pull-in position and voltages. Younis *et al* [14] presented a continuous reduced-order model for predicting the pull-in of electrically actuated MEMS micro-beams. Vogl *et al* [17] also presented a continuous reduced-order model taking into consideration a uniform residual biaxial plane stress for actuated circular plates instead of beams, as in [14]. Chao *et al* [19] proposed a novel computation procedure to predict the static pull-ins and verified it by experiments.

In addition to the above studies devoted to static pull-in, research works [27, 28] began to realize that in most practical operations of the aforementioned electrostatic devices, voltage starts to be applied when the micro-beam is not deformed, i.e., an instantaneous application (step-function) of voltage—called a dc dynamic pull-in voltage. It should be noted that most previous studies on static pull-ins [10–18, 23, 26], strictly speaking, are for 'quasi-static' pull-in prediction. For microphones and pressure sensors with an initial bias voltage applied for better performance and for micro-switches, it is very important to re-estimate the pull-in voltage with an applied voltage in the form of a step function, since the actual pull-in voltage is lower than the one predicted based on the quasi-static pull-in assumption due to the inertial effect of the deformed electrode. This pull-in at lower voltage is generally referred to as 'dc dynamic pull-in', or simply 'dynamic pull-in' by [27, 28]. For simplicity, this dc dynamic pull-in is abbreviated as 'dynamic pull-in' from now on. To predict this dynamic pull-in voltage/position, Neilson and Barbastathis [27] analyzed lumped parallel-plate and torsional electrostatic MEMS actuators. Elata and Bamberger [28] considered a lumped multiple degrees of freedom system to derive the dynamic pull-in voltage. Both works [27, 28] arrive at the ratio between static and dynamic pull-in voltages close to

91.9% for the lumped parallel-plate actuator. In order to pursue more precise dynamic pull-in predictions than those [27, 28] based on simple lumped models, the present study aims to find precise dc dynamic pull-in voltages based on a comprehensive continuous micro-beam model, even providing closed-form predictions with some level of accuracy.

Other than re-forging actuation strategies based on previous analytical works, some studies investigate the dynamics of micro-beams subjected to persistent ac voltage application [29–35], dc/ac voltage [36] and those with a time-varying capacitor [37], while others are devoted to the development of control strategies [38–42]. They use either feedback control [38–40] to prevent pull-in or a series inductance or capacitor in a control circuit [41]. A promising method is charge control [42], which successfully extends the travel range, as compared to voltage-controlled devices. Although these feedback control approaches prevent pull-in, it requires substantial effort to design and realize the control algorithm.

The present study is primarily devoted to the precise prediction of dc dynamic pull-in voltage with clear comparison with static counterparts to stress the necessity for dc dynamic pull-in voltage prediction. In order to predict the precise dc dynamic pull-in voltage, the present study starts with an establishment of continuous governing partial differential equations (PDEs) in section 2 for a micro-beam clamped at both ends. The built system PDEs are capable of describing vibrations of the micro-beam, squeeze film damping and fringing electric field effects. The Galerkin method is then employed to decompose the governing PDEs into discrete ordinary differential equations (ODEs) in section 3. The Taylor series approximation is adopted to represent the nonlinear electrostatic force term for integration in the process of Galerkin's decomposition. From the derived ODEs, the static pull-in voltages and positions are obtained via bifurcation analysis in subsection 4.1. A closed-from prediction of the static pull-in voltage is finally derived for cases of non-narrow beams. In the next step, phase portraits are depicted, where homoclinic orbits are present for system dynamic characteristics. Based on these orbits, dynamic pull-ins are predicted in subsection 4.2 and the dependence on varied beam parameters are computed and analyzed in section 5 to provide design and operation guidelines for the considered micro-beams. A closed-from prediction of the dynamic pull-in voltage is also derived for cases of non-narrow beams. Prediction results are finally validated in section 6 by finite element modeling/analysis and experimental data. Finally, section 7 concludes this study.

2. Dynamic model

A micro-beam clamped at both ends as shown in figure 1 is considered for the present study. This beam has an electrode backplate much thicker than the top micro-beam. With the application of a bias voltage across the beam and electrode backplate, a distributed electrostatic force between the beam and electrode is generated, thus deforming the micro-beam. As the applied step-like voltages increased to some level,
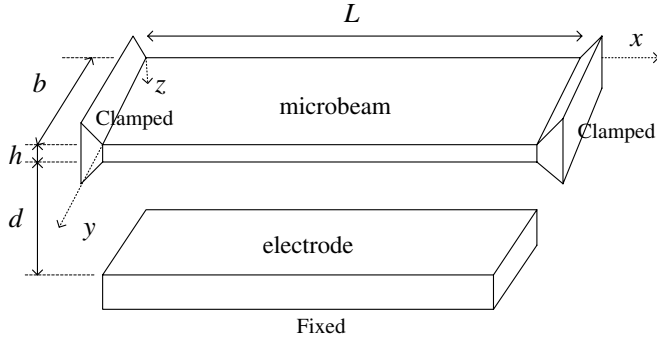
Figure 1. Cross-section and top views of the continuous model of the parallel charged micro-plates.

the restoring force induced by the deflected beam would not be able to balance the electrostatic force increased by the deformed beam, then leading to contact between the beam and electrode. This phenomenon is commonly referred to as 'pull-in' or 'pull-in instability'. For optical switches, the bias voltage is tuned to be above or below the pull-in voltage to emulate switch on and off, respectively. A precise prediction of the pull-in plays an important role in device operations. The prediction of the pull-in is started herein by establishing the governing distributed equations of motion for the top deformable thin beam in figure 1, that is,

$$E'I\frac{\partial^4 w}{\partial x^4} + \rho bh\frac{\partial^2 w}{\partial t^2} + c\frac{\partial w}{\partial t} - N\frac{\partial^2 w}{\partial x^2} = F_E - F_A, \quad (1)$$

subjected to the boundary conditions

$$w(0, t) = w(L, t) = 0, \quad (2a)$$

$$\frac{\partial w(0, t)}{\partial x} = \frac{\partial w(L, t)}{\partial x} = 0, \quad (2b)$$

where $w = w(x, t)$ is the deflection of the deformed micro-beam, x is the coordinate originated at the left beam anchor point and along the length of the micro-beam, and h, c, b and ρ are the thickness, material damping, beam width and density of the micro-beam, respectively. In addition, E' is an effective Young's modulus, i.e., $E' = E/(1 - \nu^2)$ where ν is Poisson's ratio. $A = bh$ and $I = bh^3/12$ are the cross section area and the associated moment of inertia, respectively. Finally, N denotes the axial force of the deformed beam, which can be expressed as

$$N = \sigma bh, \quad (3)$$

where σ is the residual stress arising from the heat generated during the etching process to form the deformed micro-beam. Note that the deflection of the micro-beam is small compared to its thickness; thus, the beam behavior is bending dominant. The linear stretching force by equation (3) is consequently adequate as opposed to other nonlinear stretching forces in [18] for the present study. Also appearing in the governing equation (1), F_E represents the equivalent pressure on the deformed plate due to the applied electrostatic force per unit beam length of the plate, while F_A is the equivalent pressure force per unit beam length due to the squeeze film effect.

Considering the fringing effects of the charged beam, the electrostatic force term F_E can be prescribed by [13, 20, 43]

$$F_E = \frac{\varepsilon V^2 b}{2(d - w)^2}\left[1 + 0.65\frac{(d - w)}{b}\right], \quad (4)$$

where ε, V and d are the permittivity of free space in the air gap per unit area of the deformed micro-beam, applied bias voltage and the initial air gap between the beam and the electrode, respectively. On the other hand, to obtain F_A, a 2D Reynolds equation is first derived from the Navier–Stokes equation under the assumptions that (1) the effects of air inertia are negligible as compared to viscosity, (2) the pressure gradient across the thin film is near zero and then the flow in the direction perpendicular to the plates is negligible, yielding

$$\frac{\partial}{\partial x}\left(\frac{\rho_a g^3}{12\mu}\frac{\partial p}{\partial x}\right) + \frac{\partial}{\partial y}\left(\frac{\rho_a g^3}{12\mu}\frac{\partial p}{\partial y}\right) = \frac{\partial(\rho_a g)}{\partial t}, \quad (5)$$

where μ, p, ρ_a and g represent the effective air viscosity, pressure, air density and film thickness, respectively. The effective air viscosity can be captured by $\mu = \mu_0/(1 + 6K_n)$ in order to take into account the correction on the slip-boundary condition. μ_0 is the absolute air viscosity, while K_n is the Knudsen number [44, 45] and $K_n = \lambda/g$, where $\lambda = 0.064\,\mu\text{m}$ for air. For the present study, since the air film is approximately $1\,\mu\text{m}$, K_n is small. The effective viscosity μ can then be captured by the absolute viscosity μ_0. On the other hand, based on other previous definitions, $g = d - w$. In the next step, the air in the squeeze film is assumed incompressible since the calculated squeeze numbers for the designed micro-beams listed in the tables are all small [18]. The associated pressure can further be assumed to be

$$\tilde{p} = p - p_a, \quad (6)$$

where p_a is the ambient atmospheric pressure. Following the analysis steps in [18, 46], which are essentially assuming (1) the distribution pressure as a parabolic function and (2) the gap is much smaller than the beam length, i.e., $d, g \ll L$, one can arrive at

$$F_A = -K_B\frac{\partial \hat{g}}{\partial t} \quad (7)$$

where $\hat{g} = g/d$, $K_B = (3\mu \hat{b}^2)/(2\hat{g}^3)$ and $\hat{b} = b/d$. In common practice, since $b \gg g$, K_B could be large enough such that F_A is too large to neglect in the governing equation (1), as compared to the electrostatic force term F_E. To this point, with F_E and F_A obtained in equations (4) and (7), respectively, the governing equation (1) is ready to be solved to decipher the dynamics of the deformed micro-beam. For the convenience of ensuing analysis, the system equation (1) is further nondimensionalized to be of the form

$$\frac{\partial^4 \hat{w}}{\partial \hat{x}^4} + \frac{\partial^2 \hat{w}}{\partial \hat{t}^2} + (\hat{c} + \hat{K}_B)\frac{\partial \hat{w}}{\partial \hat{t}} - \hat{N}\frac{\partial^2 \hat{w}}{\partial \hat{x}^2} = \alpha \hat{F}_E, \quad (8)$$

where

$$\hat{w} = \frac{w}{d}, \qquad \hat{x} = \frac{x}{L}, \qquad \hat{t} = \frac{t}{T}, \qquad \hat{b} = \frac{b}{d},$$

$$T = \sqrt{\frac{\rho A L^4}{EI}}, \qquad \hat{c} = \frac{cL^4}{EIT}, \qquad \hat{N} = \frac{NL^2}{EI},$$

$$\hat{F}_E = \frac{V^2}{(1-\hat{w})^2}\left[1 + 0.65\frac{(1-\hat{w})}{\hat{b}}\right], \qquad \alpha = \frac{\varepsilon b L^4}{2EId^3},$$

$$\hat{\mu} = \frac{L^4}{EIT}\mu, \qquad \hat{K}_B = \frac{\hat{\mu}\cdot\hat{b}^3}{(1-\hat{w})^3}.$$

Note in equation (8) that the beam width $\hat{b}$ affects the squeeze film effect through the term associated with $\hat{K}_B$. With a complete system equation in hand, a modal decomposition is performed in the following section to derive pull-in positions and voltages.

3. Modal equations

The method of Galerkin decomposition is employed herein to approximate the system equation (8) by a reduced-order model composed of a finite number of discrete modal equations. The process starts by separating the dependences of the deflection of the deformed thin plate, $\hat{w}(\hat{x},\hat{t})$, into temporals and spatials by the functions $\hat{w}_m(\hat{t})$s and $\phi_m(\hat{x})$s, respectively, in the form of a series of products, i.e.,

$$\hat{w}(\hat{x},\hat{t}) \approx \sum_{m=1}^{n}\hat{w}_m(\hat{t})\phi_m(\hat{x}), \qquad (9)$$

where $\hat{w}_m(\hat{t})$s capture the temporal dependence of the beam deflection by the forms of a series of time-varying coefficients, while $\phi_m(\hat{x})$s do the corresponding spatial dependence, which are the trial functions to emulate the mode shapes of the deformed thin plate with expected satisfaction of boundary conditions (2a) and (2b). Based on continuous mechanics, $\phi_m(\hat{x})$s are assumed, as below, to render well approximation even with a low number of terms (modes) considered in equation (9), i.e.,

$$\phi_m(\hat{x}) = C_0\left[\sinh(b^*\hat{x}) - \frac{b^*}{a^*}\sin(a^*\hat{x})\right.$$
$$\left. + \left(\frac{\sinh(b^*) - \frac{b^*}{a^*}\sin(a^*)}{\cos(a^*) - \cosh(b^*)}\right)(\cosh(b^*\hat{x}) - \cos(a^*\hat{x}))\right],$$
$$(10)$$

where

$$a^* = \sqrt{\frac{\sqrt{\hat{N}^2 + 4\omega_i^2} - \hat{N}}{2}}, \qquad b^* = \sqrt{\frac{\hat{N} + \sqrt{\hat{N}^2 + 4\omega_i^2}}{2}},$$

and C_0 is the coefficient to be determined. Note that N denotes the axial force and ω_is represent the ith natural frequency of the beam structure. The functions $\phi_m(\hat{x})$s in equation (10) are, in fact, the mode shapes of the considered micro-beam, and the undetermined C_0s are incorporated in $\hat{w}_m(\hat{t})$s, which are to be sought in the following computation. Substituting equation (9) into (8), multiplying by the functions $\phi_m(\hat{x})$, $1 \leqslant m \leqslant n$, in equation (10) on both sides and integrating the substituted equations over the considered surface domain of the deformed beam, the coupled nonlinear modal discrete ODEs of the system can be derived, based on mutual orthogonality between different $\phi_m(\hat{x})$s, as

$$\mathbf{M\ddot{w}} + \mathbf{C\dot{w}} + \mathbf{Kw} = \mathbf{f_e}, \qquad (11)$$

where the vector $\mathbf{w}$ contains all $\hat{w}_m(\hat{x})$s, $1 \leqslant m \leqslant n$, specified by equation (9). The elements associated with parametric matrices in equation (11) can be obtained by

$$\mathbf{M} : m_{\mathrm{mm}} = \int_0^1 \phi_m^2(\hat{x})\,\mathrm{d}\hat{x}, \qquad (12)$$

$$\mathbf{C} : c_{\mathrm{mm}} = \hat{c}\int_0^1 \phi_m(\hat{x})\cdot\phi_m(\hat{x})\,\mathrm{d}\hat{x}$$
$$+ \int_0^1 \hat{K}_B\cdot\phi_m(\hat{x})\cdot\phi_m(\hat{x})\,\mathrm{d}\hat{x} \qquad (13)$$

$$\mathbf{K} : k_{\mathrm{mm}} = \int_0^1 \left[\frac{d^4\phi_m(\hat{x})}{\mathrm{d}\hat{x}^4} - \hat{N}\cdot\frac{d^2\phi_m(\hat{x})}{\mathrm{d}\hat{x}^2}\right]\cdot\phi_m(\hat{x})\,\mathrm{d}\hat{x}. \qquad (14)$$

Also on the right-hand side of the reduced model equation (11) is the electrostatic force term $\mathbf{f_e}$, which can be derived by

$$\mathbf{f_e} : f_{\mathrm{em}} = \alpha\int_0^1 \hat{F}_E\cdot\phi_m(\hat{x})\,\mathrm{d}\hat{x} \qquad (15)$$

where $\hat{F}_E$ is the electrostatic distributive force between the beam and electrode, which is, in fact, a nonlinear function of the plate deflection $\hat{w}(\hat{x},\hat{t})$, as given in equation (8). Observing the obtained decomposed equations (11)–(14), one could arrive at the following. First, the derived k_{ii}s are the stiffness elements associated with the eigenmodes of the deformed beam. Second, the orthogonality between different modes results in diagonal matrices $\mathbf{M}$ and $\mathbf{K}$, as evidenced from the computed right-hand sides of equations (12)–(14), while matrix $\mathbf{C}$ is not diagonal due to the fact that $\hat{K}_B$ is a function of beam deflection. Therefore, the second term on the right-hand side of equation (13) results in nonzero coupling (non-diagonal) terms in matrix $\mathbf{C}$.

4. Pull-in predictions via bifurcation analysis

With the system discrete ODEs (11) in hand, bifurcation analysis is performed in this section to find static and dc dynamic pull-in voltages and positions. Note that for simplicity, this dc dynamic pull-in is abbreviated as 'dynamic pull-in' in what follows. Owing to the relative closeness between the first mode shape and practical deformed micro-beam, the analysis herein considers only the first mode in the decomposition (9), i.e., $\hat{w}(\hat{x},\hat{t}) \approx w_1(\hat{t})\phi_1(\hat{x})$, where $w_1(\hat{t})$ is then the largest deflection of the deformed fixed–fixed beam at the center point. The effectiveness of this first-mode approach to represent practical full-order micro-beam dynamics will be validated in section 6 via finite element modeling and experimental data.

4.1. Static pull-in

The static pull-in is predicted based on the dynamic equation for the first mode, as shown in equation (11). Expanding the squeeze film term associated with $\hat{K}_B$ in equation (13) and the electrostatic force term $\hat{F}_E$ in equation (15) to the Taylor series, and then incorporating them into equation (11), one

can obtain the dynamic equation for the first mode to the fifth order in a state-space form as follows:

$$\dot{\hat{x}} = \hat{y}$$
$$\dot{\hat{y}} = \gamma_0 + \gamma_1\hat{x} + \gamma_2\hat{x}^2 + \gamma_3\hat{x}^3 + \gamma_4\hat{x}^4 + \gamma_5\hat{x}^5 \quad (16)$$
$$\quad + \mu_1\hat{y} + \mu_2\hat{x}\hat{y} + \mu_3\hat{x}^2\hat{y} + \mu_4\hat{x}^3\hat{y} + \mu_5\hat{x}^4\hat{y} + \text{H.O.T.}$$

where $\hat{x} \equiv w_1$, $\hat{y} \equiv \dot{w}_1$, and H.O.T. denotes summation containing higher-order terms above the fifth order, which, based on the smallness of normalized states w_1, are omitted with satisfactory accuracy. Note that equation (16) is truncated to the fifth order for considering the nonlinear terms with order slightly higher than the first nonlinear order, the third order. This is aimed for relative accuracy in predicting beam deflection, which is basically an odd function of an applied external force. The validity of the fifth-order truncated expression (16) will be proven effective by later finite element analysis and experimental data. Performing integrations in equations (12)–(14) for Galerkin's decomposition, the parameters in equation (16) can be derived as

$$\gamma_0 = -(1.32 + 0.8576/\hat{b})\alpha V^2,$$
$$\gamma_1 = (2 + 0.65/\hat{b})\alpha V^2 - 500.544 - 12.31\hat{N},$$
$$\gamma_2 = -(2.5 + 0.544/\hat{b})\alpha V^2,$$
$$\gamma_3 = (3 + 0.4773/\hat{b})\alpha V^2, \qquad \gamma_4 = -(3.31 + 0.43/\hat{b})\alpha V^2,$$
$$\gamma_5 = (3.6447 + 0.395/\hat{b})\alpha V^2, \quad (17)$$
$$\mu_1 = -\hat{c} - 1.01\hat{\mu}\hat{b}^3, \qquad \mu_2 = 2.5\hat{\mu}\hat{b}^3,$$
$$\mu_3 = -4.406\hat{\mu}\hat{b}^3, \qquad \mu_4 = 6.62\hat{\mu}\hat{b}^3,$$
$$\text{and} \qquad \mu_5 = -9.112\hat{\mu}\hat{b}^3.$$

It can be seen from equations (16) and (17) that the electrostatic force, which is induced by the bias voltage V, influences the system dynamics through the terms with parameters γs in equation (16), while the other terms with coefficients μs are affected by the squeeze film effect and the material damping c of the deformed beam. Furthermore, the electrical field fringing affects the first-mode dynamics through the parameters $\hat{b}$s in γs. To perform bifurcation analysis, new variables $\{u \equiv \hat{x} + \gamma_1/2\gamma_2, v \equiv \hat{y}\}$ are introduced to transform equation (16) into

$$\dot{u} = v$$
$$\dot{v} = \tilde{\gamma}_1 + \tilde{\gamma}_2 u^2 + \tilde{\mu}_1 v + \tilde{\mu}_2 uv + \text{H.O.T.} \quad (18)$$

where $\tilde{\gamma}_1 \equiv \gamma_0 - \gamma_1^2/4\gamma_2$, $\tilde{\gamma}_2 \equiv \gamma_2$, $\tilde{\mu}_1 \equiv \mu_1 - \mu_2\gamma_1/2\gamma_2$ and $\tilde{\mu}_2 \equiv \mu_2$, while considering the system dynamics to the second order for bifurcation analysis. Bifurcation analysis starts by seeking the fixed-point solutions of equation (18), which can be easily derived as

$$(u, v) = (\pm\sqrt{-\tilde{\gamma}_1/\tilde{\gamma}_2}, 0) \equiv (u_\pm, 0). \quad (19)$$

Based on the definitions in equation (17), $\tilde{\gamma}_1 > 0$ and $\tilde{\gamma}_2 < 0$ for most practical designs cases in the present study; thus, the Jacobian of the system equation (18) with respect to the derived fixed-point solutions in equation (19) becomes

$$D = \begin{bmatrix} 0 & 1 \\ \pm 2\tilde{\gamma}_2\sqrt{-\tilde{\gamma}_1/\tilde{\gamma}_2} & \tilde{\mu}_1 \pm \tilde{\mu}_2\sqrt{-\tilde{\gamma}_1/\tilde{\gamma}_2} \end{bmatrix}. \quad (20)$$
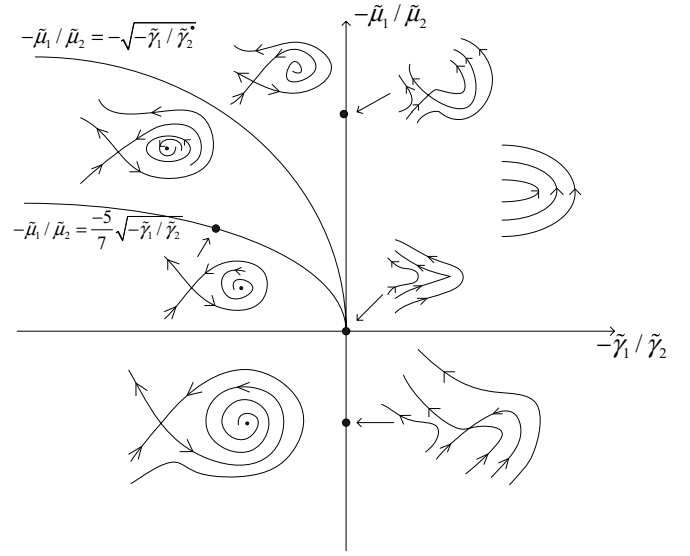

Figure 2. Bifurcation diagram.

A simple calculation with solution (19) and Jacobian matrix (20) reveals that $(u_+, 0)$ is a source for $\{-\tilde{\mu}_1/\tilde{\mu}_2 < \sqrt{-\tilde{\gamma}_1/\tilde{\gamma}_2}, \tilde{\gamma}_2 < 0, \tilde{\gamma}_1 > 0\}$ and a sink for $\{-\tilde{\mu}_1/\tilde{\mu}_2 > \sqrt{-\tilde{\gamma}_1/\tilde{\gamma}_2}, \tilde{\gamma}_2 < 0, \tilde{\gamma}_1 > 0\}$, while $(u_-, 0)$ is a saddle for $\tilde{\gamma}_2 < 0$. Checking the solution characteristics associated with the changes in the eigenvalues of D, it is found that a Hopf bifurcation occurs on the curve $\{-\tilde{\mu}_1/\tilde{\mu}_2 = \sqrt{-\tilde{\gamma}_1/\tilde{\gamma}_2}\}$, while a saddle-node bifurcation on the boundary of $\{-\tilde{\gamma}_1/\tilde{\gamma}_2 = 0, -\tilde{\mu}_1/\tilde{\mu}_2 \neq 0\}$. One can further follow the similar analysis procedures presented in [47–49] to arrive at a global bifurcation diagram, as shown in figure 2. It should be noted at this point that to describe properly the dynamic characteristics of electrostatic actuators, infinite order of the expansion should be preserved [18, 33, 37]. Furthermore, figure 2 presents only the general bifurcation results near the neighborhood of the origin, $(\hat{x}, \hat{y}) = (-\gamma_1/2\gamma_2, 0)$ based on the reduced equation (16), which do not necessarily reflect the actual responses of the full-order system. Examining the entire bifurcation diagram in figure 2, one can find that the stable fixed point at $(u_+, 0) = (\sqrt{-\tilde{\gamma}_1/\tilde{\gamma}_2}, 0)$ actually gives rise to a stable center position of the deflected micro-beam before the pull-in occurs. The disappearance of this stable $(u_+, 0) = (\sqrt{-\tilde{\gamma}_1/\tilde{\gamma}_2}, 0)$ occurs as the bias voltage increases to cross the bifurcation boundary

$$-\tilde{\mu}_1/\tilde{\mu}_2 = \sqrt{-\tilde{\gamma}_1/\tilde{\gamma}_2}, \quad (21)$$

leading to the static pull-in phenomenon. Therefore, equation (21) is, in fact, the static pull-in condition, based on which the solution of equation (21), the static pull-in voltage, can be obtained. However, due to its complexity, the expression of this static pull-in voltage is only listed in the appendix. The associated pull-in position can then be derived by incorporating condition (21) into $(u_+, 0) = (\sqrt{-\tilde{\gamma}_1/\tilde{\gamma}_2}, 0)$, yielding, after simplification,

$$w_{1,pi} \approx \frac{\sqrt{0.340\,04/\hat{b} + 0.523\,138}}{\sqrt{0.215\,742/\hat{b} + 0.995\,732}}, \quad (22)$$

where the micro-beam material damping c is considered small as compared to the squeeze film effect and then neglected. Note that the resulting static pull-in voltage and position from equations (21) and (22) are not exact, since they are derived only based on the truncated dynamics of the original equation (16) up to the second order. To increase prediction precision, the higher order terms in equation (16) are considered to solve for pull-in voltage/position. However, limited by the computation capability of manipulating complicated equations, the closed-form prediction of the static pull-in voltage can only be derived up to the fourth order. Due to its lengthy expression, it is not reported here. For better precision in predictions, equation (16) up to the fifth order are directly solved for steady-state solutions and then the associated Jacobian is computed for deriving bifurcation condition, which leads to numerical solutions of static pull-in position/voltages. These fifth-order solutions could be used to explore the correctness of the previously derived low-ordered solution. It is pertinent to note at this point that the previous lengthy solutions are primarily due to the consideration of field fringing effects. Without taking fringing effects into consideration, the static pull-in voltage can be solved to the fifth order in a closed-form as follows:

$$V_{s,pi} \approx \frac{0.927\,783\sqrt{82.2287 + 2.021\,65\hat{N}}}{\sqrt{\alpha}}, \quad (23)$$

where the subscripts stand for 'static pull-in'. The associated pull-in deflection is

$$w_{1,pi} \approx 0.414311, \quad (24)$$

which is close to those static pull-in predictions in [13–19]. Finally, full-order solutions are also sought based on equation (11) and following the detailed procedure provided by [19], which adopts the well-known numerical approaches of Simpson's integration and Newton's method for solving nonlinear algebraic equations on the right-hand sides of equation (11).

Based on the aforementioned solution process, figures 3(*a*) and (*b*) depict the resulting static pull-in voltages and positions, respectively, with respect to the varied normalized beam width $\hat{b}$. This normalized parameter $\hat{b}$ is actually the ratio of actual beam b width to the gap d. Based on figure 3, the effects of the fringing field can be derived, which generally follows those discovered by the analysis in [20]. It is seen from figure 3(*a*) that the derived static pull-in voltages in cases without fringing effects considered do not depend on the beam width, while in cases with field fringing considered the pull-in voltages are smaller at low $\hat{b}$, but approach those without field fringing considered as $\hat{b}$ increased. Based on the above observation, it can be deduced that if the width of the micro-beam considered is narrow, i.e., approximately $\hat{b} < 30$, the fringing field effects should be considered to render accurate predictions on static pull-in voltages; otherwise, the static pull-in voltage could be approximated well by the fifth-order approximation in equation (23), which is in a closed form. It is also seen from figure 3(*a*) that the static pull-in voltages with field fringing considered decreases substantially as the beam width is close to zero (for narrow beams). This is due to the fact that the field fringing effect is strong for narrow
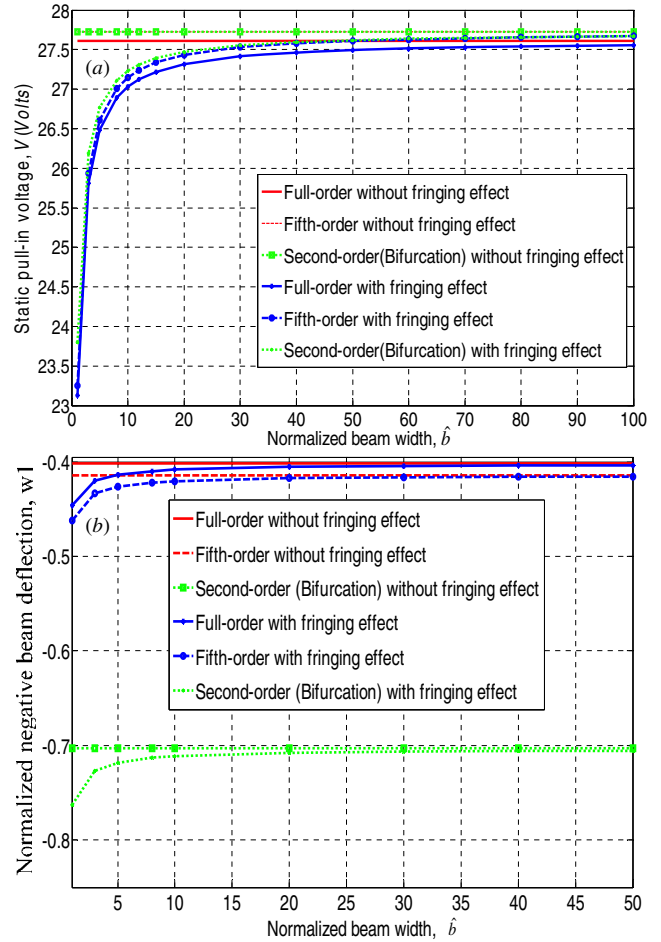

Figure 3. (*a*) Static pull-in voltages and (*b*) the associated center deflection (downward), with respect to the beam width $\hat{b}$.

beams, thus causing earlier pull-ins at small levels of applied voltages.

Regardless of whether field fringing is considered or not, it is seen from figure 3(*a*) that the fifth-, full-order and second-order (bifurcation results from equation (21)) predictions are close to each other, while the second-order has slightly higher predictions, indicating that the second-order predictions might not be the suitable choices for designers to seek precise pull-in voltages. However, it should be recalled that compared to the results in the literature [13–19] where lumped models or low-order predictions are performed, predictions without fringing effects considered still present a fair correctness for the MEMS micro-beam designer, while $\hat{b}$ is above the moderate level. On the other hand, figure 3(*b*) shows the corresponding center deflection of the micro-beam at the occurrence of pull-in, where it is also seen that second-order (bifurcation) analysis predicts much larger pull-in deflections (in magnitude) than fifth- and full-orders, indicating that second-order deflection predictions are not reliable.

4.2. Dynamic pull-in

Analysis of the transient response is pertinent at this point, since for common operations of micro-beam devices a bias

voltage is applied when the beam is not deformed, i.e., $\hat{w}(\hat{x}, 0) = 0$. Besides, the beam inertia and viscosity arising from the squeezed film in the gap play a part in dynamic pull-in occurrence. Therefore, the pull-in voltage has to be re-estimated with the micro-beam dynamics considered. Note that the corresponding bias voltage leading to the pull-in is defined herein as 'the dynamic pull-in voltage' [27, 28]. The related deformation of the beam as the pull-in occurs is called "dynamic pull-in deformation (roughly 'position')". Based on the above-defined dynamic pull-in, the associated pull-in voltage is sought to be smaller than static counterparts derived by equation (21). To find an exact prediction of the dynamic pull-in, the related position/voltage are then derived based on the Hamiltonian formulation and homoclinic bifurcation analysis. This process starts by assuming that the air viscosity in the squeezed film and the material damping of the deformed beam are small; thus, the parameters μs defined in equation (17) are small, enabling the scaling of $\mu = \varepsilon\bar{\mu}$, which can be utilized to re-express the truncated state equation (18) as

$$\dot{u} = v$$
$$\dot{v} = \tilde{\gamma}_1 + \tilde{\gamma}_2 u^2 + \varepsilon\left(\bar{\mu}_1 v + \bar{\mu}_2 uv\right) + \text{H.O.T.}$$

(25)

With the above scaled equations, the bifurcation problem is reduced to a two-parameter problem with a small scaling parameter ε. Considering $\varepsilon \to 0$, i.e., zero dampings, equation (25) becomes an integrable Hamiltonian system

$$\dot{u} = v$$
$$\dot{v} = \tilde{\gamma}_1 + \tilde{\gamma}_2 u^2$$

(26)

with the Hamiltonian

$$H(u, v) = \frac{v^2}{2} - \tilde{\gamma}_1 u - \frac{\tilde{\gamma}_2}{3} u^3.$$

(27)

The motivation for introducing an unperturbed (undamped) system in equation (26) is to predict the occurrence of the dynamic pull-in first based on this simpler system; thus, the precise dynamic pull-in could be derived by extending the results to the perturbed system. Typical phase portraits of the above unperturbed system near the dynamic pull-in can easily be depicted, which are shown in figure 4 for before, at and after the dynamic pull-in. The parameters of a typical micro-beam listed in table 1 are used for calculations to generate figure 4. Note that figure 4 is presented in the axes of pre-defined $\hat{x} = w_1$ and $\hat{y} = \dot{w}_1$, different from u and v in equation (25), for an easy ensuing analysis. It is seen from figure 4 that there is a particular orbit Γ_0 originating from and ends at a saddle point S, which is called the 'homoclinic orbit'. Based on the theory for classic Hamiltonian systems, the value of the Hamiltonian H defined in equation (27) is preserved along an orbit. Since this orbit passes the equilibrium of the system equation (26), the saddle point in figure 4, the following can be obtained:

$$H^{\Gamma_0}(u, v) = 4(\tilde{\gamma}_1)^{3/2}/3(-\tilde{\gamma}_2)^{1/2},$$

(28)

which is a positive real number since $\tilde{\gamma}_2$ is negative. While looking for dynamic pull-ins, we need to determine whether

Table 1. Typical baseline parameter values of the micro-beam for pull-in analysis [22].

Symbol	Parameters	Value/unit
h	Beam thickness	3.0 μm
L	Beam length	350.0 μm
d	Gap thickness	1 μm
b	Beam width	50 μm
E	Young's modulus	169 GPa
σ	Residual stress	40 MPa

the orbit starting from the origin of figure 4, $(\hat{x}, \hat{y}) \equiv (w_1, \dot{w}_1) = (0, 0)$, is located inside the homoclinic orbit Γ_0. It is seen from figure 4(*a*) that with a smaller bias voltage, the origin is located inside Γ_0, the consequent dynamics starting from the origin oscillates and never diverges outside of the homoclinic orbit Γ_0, i.e., no pull-in occurs. In contrast, if the bias is increased, the homoclinic orbit Γ_0 moves to the left direction in the phase portrait, as shown in figures 4(*a*)–(*c*), until Γ_0 is outside of the origin, causing dynamic pull-in. Therefore, it can be concluded that the dynamic pull-in occurs when the homoclinic orbit Γ_0 passes $(\hat{x}, \hat{y}) \equiv (w_1, \dot{w}_1) = (0, 0)$, or $(u, v) = (\gamma_1/2\gamma_2, 0)$. The corresponding dynamic pull-in voltage can be found by solving

$$4(-\tilde{\gamma}_1)^{3/2}/3(\tilde{\gamma}_2)^{1/2} = H^{\Gamma_0}\left(u = \frac{\gamma_1}{2\gamma_2}, v = 0\right).$$

(29)

Due to high nonlinearity involved in equation (29), only numerical solutions of the dynamic pull-in voltage can be obtained. It should be noted at this point that since the dynamic pull-in prediction based on equation (29) results from the previous zero-dissipation assumption, the solved dynamic pull-in voltage is, in fact, the lower bound of the true value. On the other hand, if the field fringing effects are neglected, a much simpler closed-form of the dynamic pull-in voltage can be derived to the fifth-order terms of the original expanded equation (16), which is

$$V_{d,pi} = \frac{0.777\,372\sqrt{99.2355 + 2.439\,78\hat{N}}}{\sqrt{\alpha}},$$

(30)

where the subscripts stand for 'dynamic pull-in'. Note that the derived dynamics pull-in voltage in equation (30) is in a similar form to its static counterpart in equation (23), but with different parameter values.

In addition to using truncated equations for predicting the dynamic pull-in voltage, one can perform direct simulation on the reduced-order governing equation (11) for the first mode via the well-known Runge–Kutta method to find the full-order dynamic pull-in voltages. This process can be illustrated by the related phase portraits, as shown in figure 4, where two equilibria $\{F, S\}$ and a homoclinic orbit Γ_0 are present. In these figures, F is a sink while S is a saddle. First, considering a voltage level well under the possible range of pull-in voltage, the location of S is solved based on equation (16). Second, taking S as the initial states, equation (16) are simulated backward in time to generate the homoclinic orbit Γ_0 as shown in figure 4(*a*) and then find its intersection with the horizontal axis. If the intersection is relatively right to the origin of figure 4, the rest position
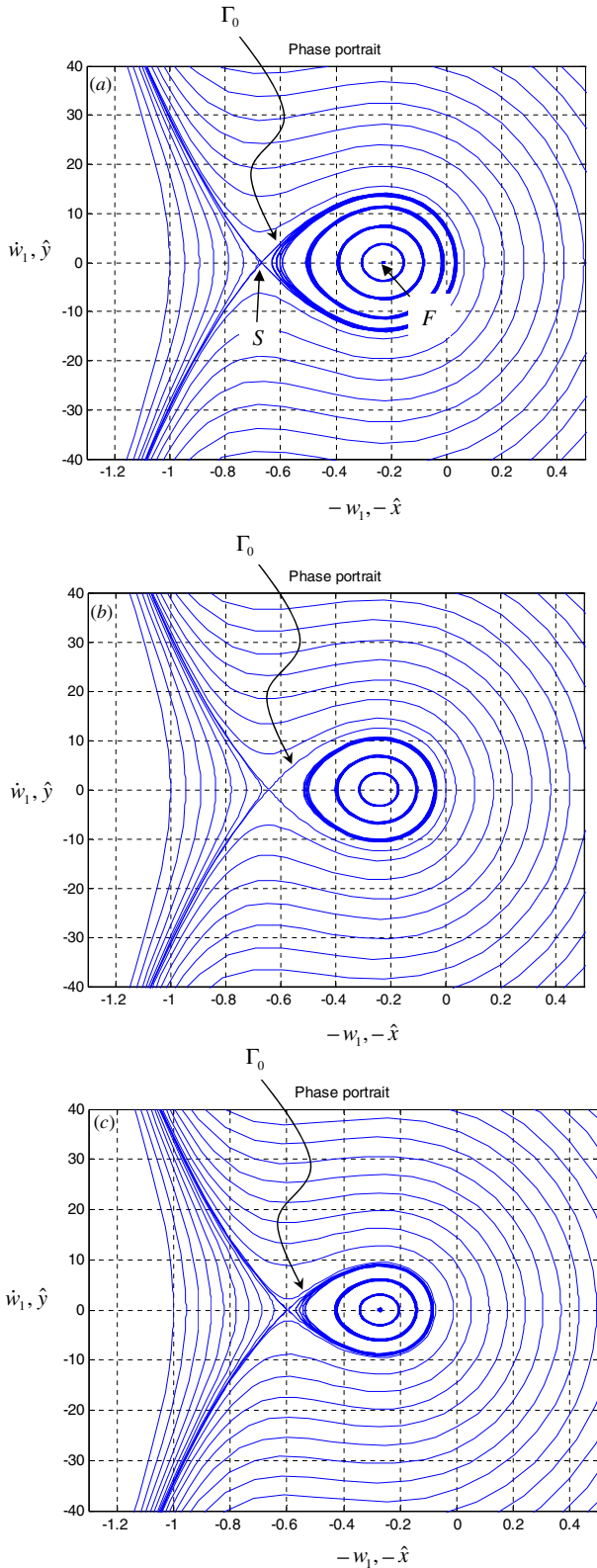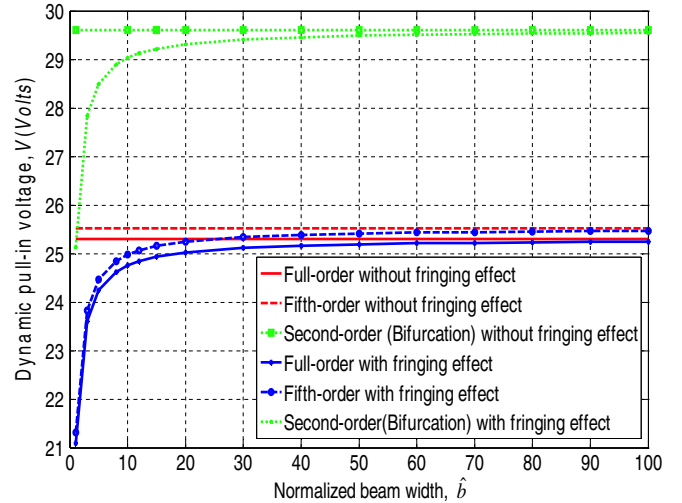
Figure 5. Dynamic pull-in voltages.

With the previous methods developed, the dynamic pull-in voltages can now be calculated and then depicted versus the beam width $\hat{b}$, as shown in figure 5. Note that the normalized parameter $\hat{b}$ is actually the ratio of the actual beam b width to the gap d, as defined in equation (2a). It is seen from figure 5 that the fifth- and full-order dynamic pull-in voltage predictions are close to each other and both lead to substantially smaller dynamic pull-in voltages than the second-order (bifurcation) predictions. Therefore, for accurate and safe operations, only the fifth- or full-order predictions are recommended to approximate the dynamic pull-in voltage. On the other hand, for all order results, the predictions with fringing effects considered are close to those without only in a range of higher beam width, indicating that if the width of the micro-beam considered is narrow, i.e., approximately $\hat{b} <$ 30, the fringing field effects should be considered to render accurate predictions on dynamic pull-in voltages; otherwise, the dynamic pull-in voltage could be approximated well by the closed-form expression (30).

5. Prediction results

With the prediction methods well established in the last section, the pull-in voltage is calculated with respect to varied parameters of the micro-beam in this section, aiming to distill design guidelines for micro-beam-type MEMS devices. The parameters listed in table 1 are used as baseline parameter values in the following analysis with some key parameters varied.

Figure 6(a) depicts the dependence of the pull-in voltage on the beam length L for four different cases: (1) static pull-in voltage; (2a) dynamic pull-in voltage; (3) dynamic pull-in voltage with fringing effects considered; (4) dynamic pull-in voltage with fringing and further squeeze film effects considered. Figure 6(b) shows the ratio of the three aforementioned predicted dynamic pull-in voltages to static counterparts. First seen from figure 6(a) is that the static pull-in voltages are clearly larger than all the other three dynamic
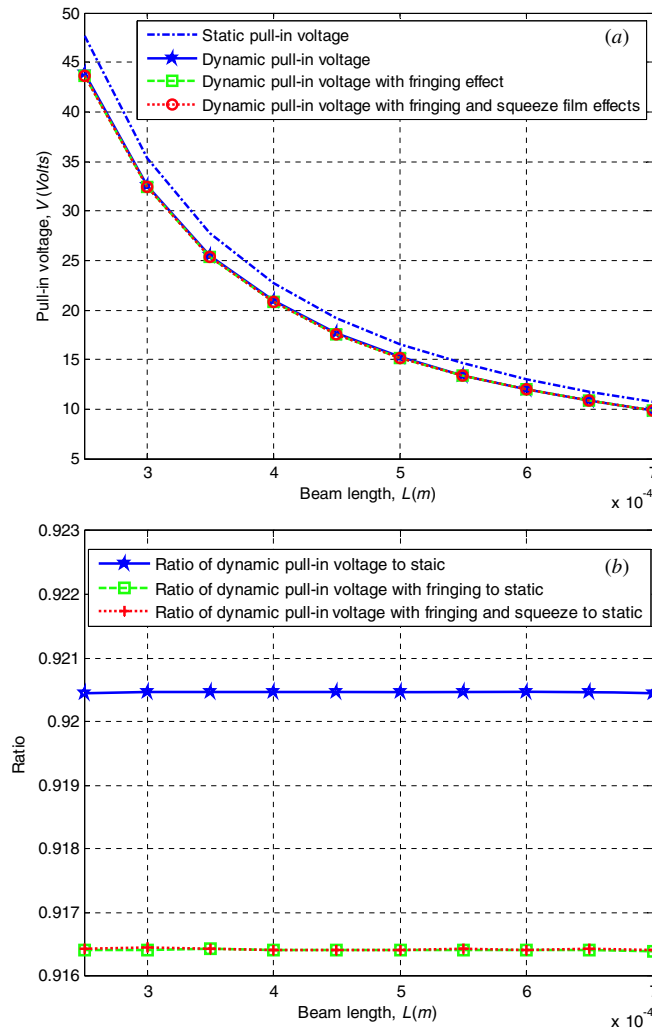
Figure 4. Typical phase portraits: (a) before the dynamic pull-in, $V < V_{d,pi}$; (b) at the dynamic pull-in, $V = V_{d,pi}$; (c) after the dynamic pull-in, $V > V_{d,pi}$.

of the vibrating beam, the voltage is increased to repeat the simulation process until the voltage level leads to the intersection at the origin, as shown in figure 4(b). The final voltage level is the 'full-order' pull-in voltage.

Figure 6. (*a*) Pull-in voltage versus micro-beam length; (*b*) the ratio of dynamic to static pull-in voltages.

Figure 7. (*a*) Pull-in voltage versus micro-beam width; (*b*) ratios of dynamic to static pull-in voltages.

ones regardless of beam length, while all of them decrease as the beam length increases, which is due to an increase in beam flexibility regarding tip displacement. Also seen from figure 6(*a*) is the closeness between three differently predicted dynamic pull-in voltages, indicating that as the beam length changes, the electric field fringing and squeeze film effects do not significantly affect the dynamic dc pull-in voltage due to the change in beam length. On the other hand, the ratios presented in figure 6(*b*) are seen all below one and around 91–92%, among which the cases considering the compete effects of field fringing and squeeze film lead to 91.64%, which is close to those predictions in past theoretical studies [27, 28]. The reason why the ratio is below one is that dynamic pull-in should occur at a lower level than its static counterpart. This alerts designers that they should avoid the pull-in much earlier than the commonly acknowledged one-third of the gap, the static pull-in position.

Figure 7(*a*) depicts the dependence of the pull-in voltage on the beam width *b* for the four different cases identical to those in figure 6, while figure 7(*b*) shows the ratio of the dynamic to static pull-in voltage for cases with and without fringing effects considered. Note that although some of the
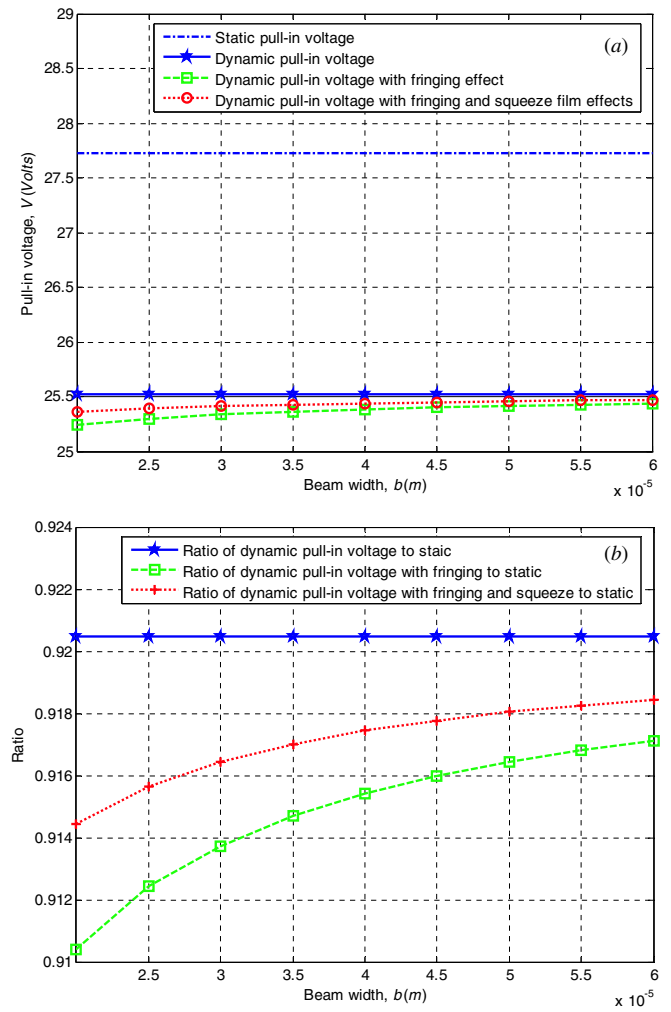
information shown in figure 7 is seen in figures 3 and 5, the latter two figures are plotted with the primary focus on discussing the legitimacy of the different computation methods applied in this study to find pull-in voltages, while figure 7 is depicted to show the relevance between the static and dynamic pull-in voltages and their dependences on the beam width. It is seen from figure 7(*a*) that without considering fringing and squeeze film effects, both static and dynamic pull-in voltage are constants, as shown in figure 7(*a*), reflecting the fact that the beam width does not affect the pull-in phenomenon unless the fringing effect and/or squeeze film are considered. Once they are considered, the pull-in voltage is increased while the beam width increases, to a value close to that of the dynamic pull-in without fringing and/or squeeze film effects considered. Another observation seen from figure 7(*a*) is that the case with squeeze film considered renders larger (safer) dc dynamic pull-in voltage than that without squeeze film. Figure 7(*b*) shows, on the other hand, that the ratios of dynamic to static pull-in voltages are below one and around 91–92%, among which the ratio resulting from the complete effects of field fringing and squeeze film increases to approximately 91.72% as the beam width increases.
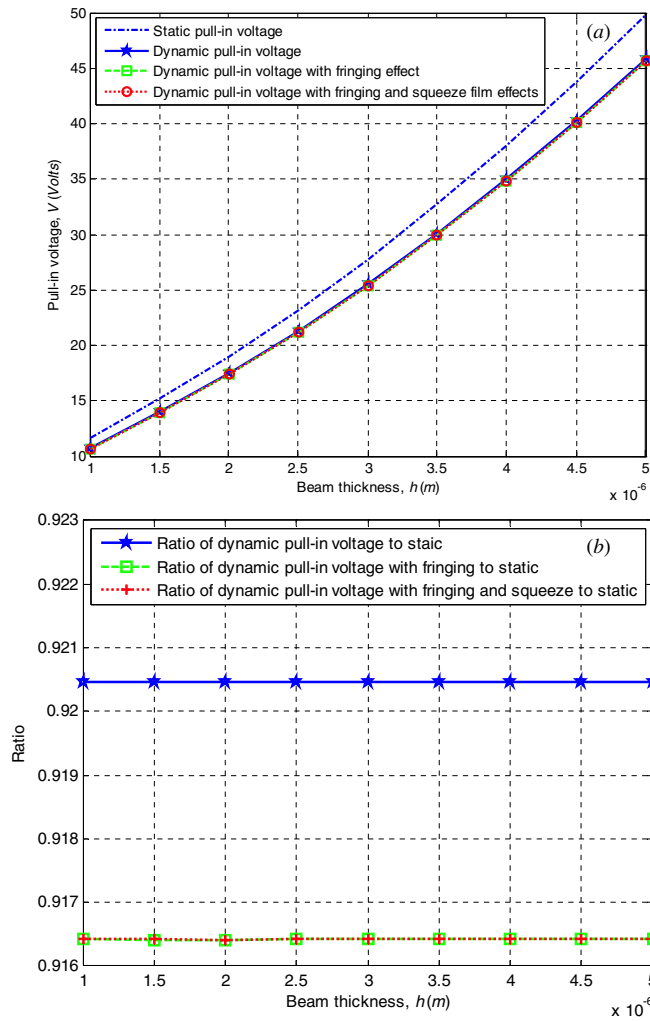
Figure 8. (*a*) Pull-in voltage versus micro-beam thickness; (*b*) ratios of dynamic to static pull-in voltages.

Table 2. Parameter values of the micro-beam for static pull-in analysis [22].

Symbol	Parameters	Value/unit
h	Beam thickness	2.94 μm
d	Gap thickness	1.05 μm
b	Beam width	50 μm
E	Young's modulus	138 GPa
σ	Residual stress	10 MPa

Figure 8(*a*) depicts the dependence of the pull-in voltage on the beam thickness h for the four different cases identical to those in figure 8, while figure 8(*b*) shows the ratio of the dynamic to static pull-in voltage for cases with and without fringing effects considered. It is seen from figure 8(*a*) that all three dynamic pull-in voltages are close to each other and clearly smaller than the static counterpart. As the beam thickness increases, all pull-in voltages are increased due to an increase in beam flexural rigidity. On the other hand, the ratios of dynamic to static pull-in voltages, as shown in figure 8(*b*), are kept around 91–92% as constants, among which the cases considering compete effects of field fringing and squeeze film leads to 91.64%.
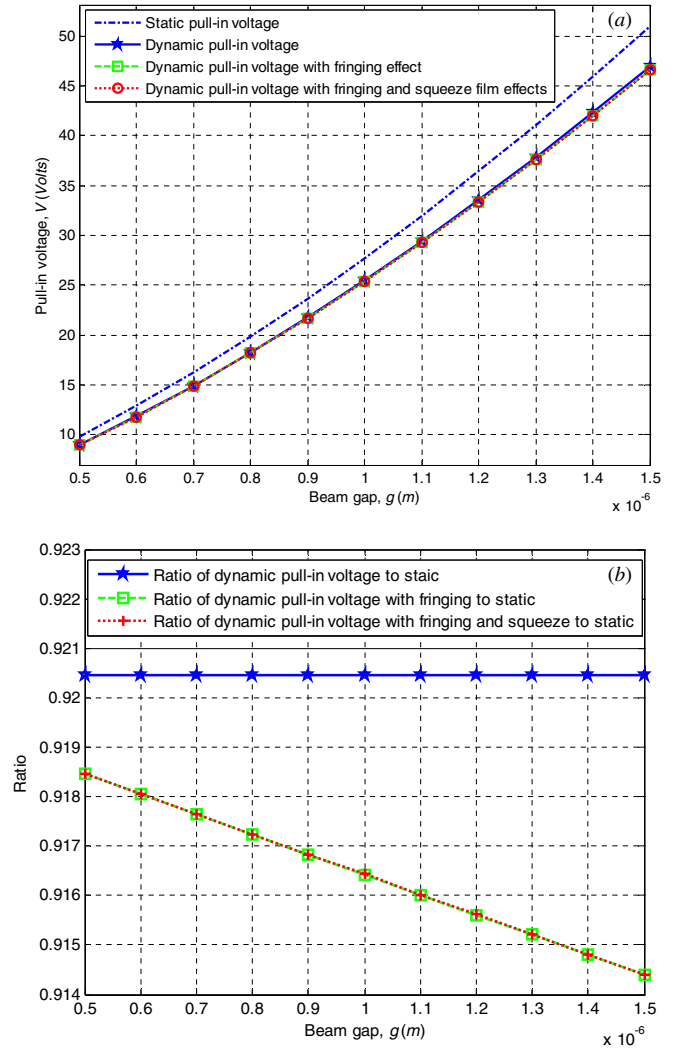

Figure 9. (*a*) Pull-in voltage versus the micro-beam gap; (*b*) ratios of dynamic to static pull-in voltages.

Table 3. Parameter values of the micro-beam for dynamic pull-in analysis [19].

Symbol	Parameters	Value/unit
h	Beam thickness	2.2 μm
L	Beam length	610.0 μm
d	Gap thickness	2.3 μm
b	Beam width	40 μm
E	Young's modulus	149 GPa
σ	Residual stress	-3.7 MPa

Figure 9(*a*) depicts the dependence of the pull-in voltage on the air gap g for the four different cases identical to those in figure 7, while figure 9(*b*) shows the ratio of the dynamic to static pull-in voltage for cases with and without fringing effects considered. It is seen from figure 9(*a*) that three dynamic pull-in voltages are close to each other and clearly smaller than the static counterpart; furthermore, among three dynamic pull-in voltages, the case without fringing effects and squeeze film considered renders the largest pull-in voltage, while the case considering both fringing and squeeze film effects leads to the smallest pull-in voltage, the easiest case to induce pull-in. On
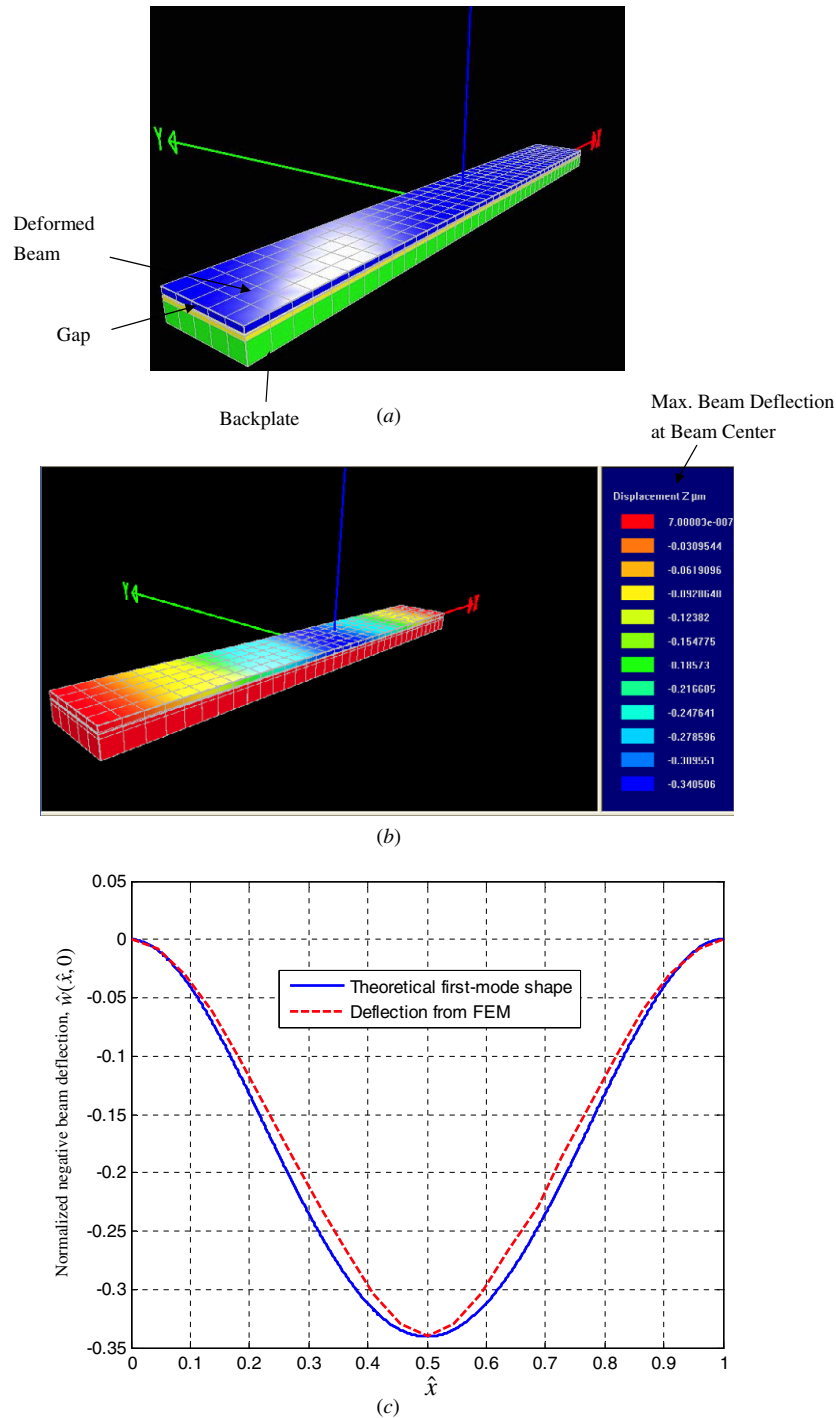
Figure 10. (*a*) The established micro-beam FEM model; (*b*) computed deflection of the thin plate by the FEM model; (*c*) the theoretical first mode shape and FEM micro-beam deflection in normalized fashion, $-\hat{w}(\hat{x}, 0)$.

the other hand, it is clearly seen from figure 9(*b*) that as the gap increases, the ratio with field fringing and/or squeeze film considered decreases, which is due to the fact that an absolute increase in the gap means a decrease in the normalized beam width $\hat{b}$, resulting in decreases in the ratio due to the effect of field fringing intensifies. On the other hand, it is clear from figure 9(*b*) that the effect of the squeeze film does not play a more important role than field fringing. Based on the above, it is suggested that the designer has to consider the effects

of field fringing while utilizing the pull-in phenomenon for operation.

6. Validation

The pull-in voltages and positions predicted in the previous section are validated herein by (1) finite element modeling and (2*a*) experimental data.
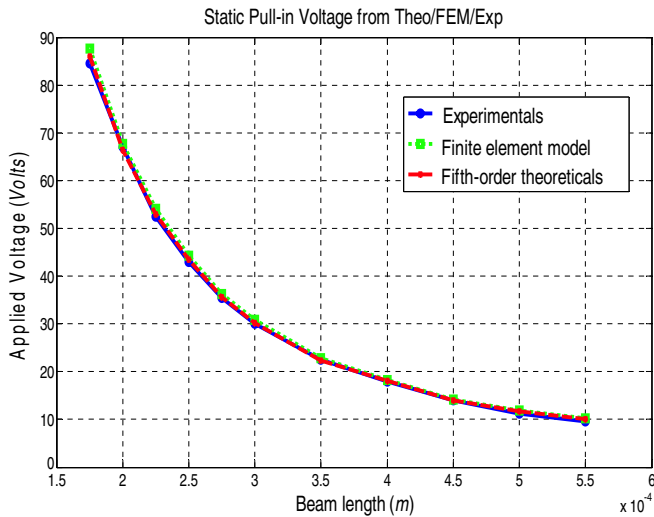
Figure 11. Comparison of static pull-in voltages between experimental and theoretical studies.

Figure 12. Comparison of dynamic pull-in voltages between experimental and theoretical studies.

In addition to the theoretical continuous model presented in section 1, a finite element model (FEM) is established to predict the micro-beam deflection, the results of which are supposed to be close to those based on finite-order approximations and the first mode derived in section 4, in order to justify all the previous reduced-order approximations. The modeling is accomplished using a commercial FEM package, Intellisuite [50]. The required analysis falls in the category of a coupled-field system of mechanical and electrical ones. For computation, two approaches, the sequential and direct methods, are offered by Intellisuite to solve the problem. The direct method is adopted in this study for less error.

Figure 10(*a*) shows the configuration of the established FEM micro-beam model. Figure 10(*b*) presents the computed deflection of the thin beam by the FEM model with a 50 V bias voltage applied and the parameters values listed in table 1 for a typical micro-beam. Note that the computation is completed with the convergence criterion set to 0.0001 um. It is seen that the deflection reaches 0.34 μm at the center position of the deformed beam. Figure 10(*c*) shows the downward (negative $\hat{w}(\hat{x}, 0)$ for easy visualization) normalized plate deflection along the *x* axis and its counterpart predicted by the first-mode approximation presented in equation (10). General closeness is clearly seen between the deflection profiles. The results obtained validate the effectiveness of the first-mode approximation to predict the pull-in phenomenon. Therefore, the established FEM model would be utilized further for validating the correctness of the previous predictions derived from bifurcation.

With theoretical predictions and finite element modeling accomplished, a comparison between varied predictions and experimental data reported in the previous literature is performed. Figure 11 presents the static pull-in voltages from experiments [43], the fifth-order predictions from section 4.1, and finite element modeling, where it is seen that three series of predictions are extremely close to each other, showing the validity of the fifth order predicted in section 4.1. Note that the parameters of the micro-beam considered are
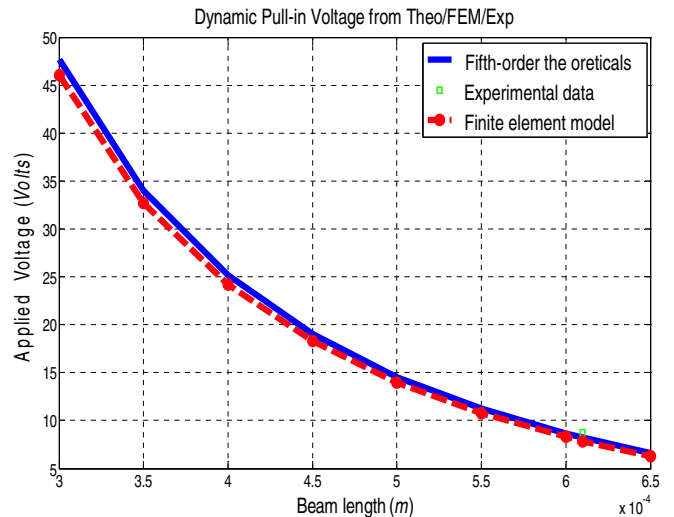
those considered in [43], as listed in table 2. On the other hand, figure 12 presents the dynamic pull-in voltages, where the single experimental data come from the study [26]. The parameters are those in table 3, which are obtained from [26]. It is seen from this figure that the single experimental data are close to its counterparts from the fifth-order predictions and finite element model, showing again that the method of the fifth-order dynamic pull-in approximation established in section 4.2 is capable of reaching fairly accurate prediction of the dynamic pull-in voltage. Therefore, users of MEMS devices in the structure of a deformed micro-beam could follow the prediction procedure provided by the present study to avoid dynamic pull-in.

7. Concluding remarks

The techniques of bifurcation and phase portrait analyses are utilized in this study to predict dc dynamic and static pull-in voltages. This study offers designers and operators of MEMS micro-beam devices a precise prediction of dc dynamic and static pull-in voltage, since the resulting voltage is derived from continuous modeling of the micro-beam, modal analysis, and followed by bifurcation and state-space analysis on the modal equations with high-order terms. The aforementioned analytical approaches are further validated by finite element analysis via Intellisuite and some experimental data in the literature. The following conclusive remarks are presented:

(1) The static pull-in center position of the micro-beam derived in this study based on bifurcation analysis to the fifth-order term is about 41% of the gap, as shown in equation (24), which is the same as those in past studies [13–19]. Furthermore, this fifth-order approximation is shown as a valid choice as compared it to full-order analysis, finite element analysis and experimental data in the literature. With a non-narrow beam being considered, i.e. the ratio of actual beam width to the gap exceeds 30, an accurate closed-form expression of static pull-in

voltage is provided by fifth-order analysis and neglecting field fringing.

(2) The dc dynamic pull-in voltage is also derived in this study by bifurcation and phase-portrait analyses. The derived dynamic pull-in voltage is found around 91–92% of the static pull-in counterpart, depending on varied parameters of the micro-beam. This is, of course, indicates an earlier dc dynamic pull-in than static case. The derived dc dynamic pull-in voltage is also close to past theoretical studies on the dynamic pull-in voltage [27, 28], where only lumped models are considered. With a non-narrow beam being considered, i.e. the ratio of actual beam width to the gap exceeds 30, an accurate closed-form expression of dynamic pull-in voltage is provided by fifth-order analysis and neglecting field fringing.

(3) Taking advantage of considering the continuous model in this study, the dependence of pull-in voltage on varied micro-beam parameters is explored. In compliance with physical intuition, it is found that the dc dynamic pull-in voltage increases with increases in beam thickness and air gap, but decreases as the beam length increases.

(4) While exploring the dependence of the dc dynamic pull-in voltage to micro-beam width, it is found that the beam width does not affect the pull-in voltage until the effect of electric field fringing and squeeze film is considered. This is all due to the fact that a decrease in beam width strengthens the field fringing, causing an earlier pull-in. Therefore, the narrower the beam is, the smaller the dc dynamic pull-in voltage is.

The study could be extended in the future to conduct experiments for a series of data to confirm the prediction about dc dynamic pull-in voltages, and also to consider different shapes and structures of MEM capacitor-type devices, such as circular or square types, to derive expressions for the dc dynamic pull-in voltage.

Acknowledgments

Appendix

The expression of the static pull-in voltage found based on Hopf bifurcation is

$$V_{s,pi} = \sqrt{ -\frac{2\tilde{b}(-2.69\times10^{15}-6.62\times10^{13}\hat{N})}{\alpha\cdot(-0.1763\times10^{13}\tilde{c}^2+2.69\times10^{12}\tilde{b}^2-1.08\times10^{13}\tilde{a}\tilde{c})} +2\cdot\sqrt{\frac{\tilde{b}^2(-2.69\times10^{15}-6.62\times10^{13}\hat{N})^2}{\alpha^2(-0.1763\times10^{13}\tilde{c}^2+2.69\times10^{12}\tilde{b}^2-1.08\times10^{13}\tilde{a}\tilde{c})^2} -\frac{4(6.74\times10^{17}+3.31\times10^{16}\hat{N}+4.08\times10^{14}\hat{N}^2)}{\alpha^2(-0.1763\times10^{13}\tilde{c}^2+2.69\times10^{12}\tilde{b}^2-1.08\times10^{13}\tilde{a}\tilde{c})}} }$$

where

$$\tilde{a} = -(1.32 + 0.8576/\hat{b}),$$
$$\tilde{b} = (2 + 0.65/\hat{b}),$$
$$\tilde{c} = -(2.5 + 0.544/\hat{b}).$$

References

[1] Ho J J, Fang Y K, Hsieh M C, Ting S F, Chen G S, Ju M S, Chen T Y, Huang C R and Chen C Y 2000 Development of a microelectromechanical system pressure sensor for rehabilitation engineering applications *Int. J. Electron.* **87** 757–67

[2] Sallese J M, Grabinski W, Meyer V, Bassin C and Fazan P 2001 Electrical modeling of a pressure sensor MOSFET *Sensors Actuators* **94** 53–8

[3] Pedersen M, Olthuis W and Bergveld P 1997 A silicon condenser microphone with polymide diaphragm and backplate *Sensors Actuators* **63/2** 97–104

[4] Pedersen M, Olthuis W and Bergveld P 1998 High-performance condenser microphone with fully integrated CMOS amplifier and DC-DC voltage converter *J. Microelectromech. Syst.* **7** 387–94

[5] Chik K D 1997 Precision wavelength light sources for dense WDM system *Proc. SPIE Int. Soc. Opt. Eng.* **12** 972–8

[6] Liu A Q, Zhang X M and Tang D Y 2002 MEMS widely tunable lasers for WDM system applications *Proc. SPIE Int. Soc. Opt. Eng.* **4907** 186–94

[7] Zhang X M, Liu A Q and Ang D Y 2002 MEMS variable optical attenuator using low driving voltage for DWDM systems *Electron. Lett.* **38** 382–3

[8] Jiang L, Shi Y, Ding Y, Lai Z and Zhu Z 2005 Numerical analysis of pull-in voltage for contact MEMS switches in switched-line phase shifter application *Proc. SPIE Int. Soc. Opt. Eng.* **5774** 587–90

[9] Zhu Y and Espinosa H D 2004 Effect of temperature on capacitive RF MEMS switch performance—a coupled-field analysis *J. Micromech. Microeng.* **14** 1270–9

[10] Batra R C, Porfiri M and Spinello D 2007 Review of modeling electrostatically actuated microelectromechanical systems *Smart Mater. Struct.* **16** R23–31

[11] Nadal-Guardia R, Brosa A M and Dehe A 2003 AC transfer function of electrostatic capacitive sensors based on the 1D equivalent model: application to silicon microphones *J. Microelectromech. Syst.* **12** 972–8

[12] Nadal-Guardia R, Brosa A M and Dehe A 2003 Constant charge operation of capacitor sensors based on switched-current circuits *IEEE Sens. J.* **3** 835–42

[13] Cheng J, Zhe J and Wu X T 2004 Analytical and finite element model pull-in study of rigid and deformable electrostatic microactuators *J. Micromech. Microeng.* **14** 57–68

[14] Younis M I, Abdel-Rahman E M and Nayfeh A H 2003 A reduced-order model for electrically actuated microbeam-based MEMS *J. Microelectromech. Syst.* **12** 672–80

[15] Nayfeh A H and Younis M I 2004 A newapproach to the modeling and simulation of flexible microstructures under the effect of squeeze-film damping *J. Micromech. Microeng.* **14** 170–80

[16] Nayfeh A H and Younis M I 2004 Modeling and simulations of thermoelastic damping in microplates *J. Micromech. Microeng.* **14** 1711–7

[17] Vogl G W V and Nayfeh A H 2005 A reduced-order model for electrically actuated clamped circular plates *J. Micromech. Microeng.* **15** 684–90

[18] Krylov S and Maimon R 2004 Pull-in dynamics of an elastic beam actuated by continuously distributed electrostatic force *J. Vib. Acoust* **126** 332–42

[19] Chao P C P, Chiu C W and Tsai C Y 2006 A novel method to predict the pull-in voltage in a closed form for micro-plates actuated by a distributed electrostatic force *J. Micromech. Microeng.* **16** 986–98

[20] Batra R C, Porfiri M and Spinello D 2006 Capacitance estimate for electrostatically actuated narrow microbeams *Micro Nano Lett.* **1** 71–3

[21] Pamidighantam S, Puers R, Baertand K and Tilmans H A C 2002 Pull-in voltage analysis of electrostatically actuated beam structures with fixed–fixed and fixed–free end conditions *J. Micromech. Microeng.* **12** 458–64

[22] Xie W C, Lee H P and Lim S P 2003 Nonlinear dynamic analysis of MEMS switches by nonlinear modal analysis *Nonlinear Dyn.* **31** 243–56

[23] Oberhammer J, Liu A Q and Stemme G 2007 Time-efficient quasi-static algorithm for simulation of complex single-sided clamped electrostatic actuators *J. MEMS* **16** 373–82

[24] Choi B and Lovell E G 1997 Improved analysis of microbeams under mechanical and electrostatic loads *J. Micromech. Microeng.* **7** 24–9

[25] Gaspar J, Chu V and Conde J P 2003 Electrostatic actuation of thin-film microelectromechanical structures *J. Appl. Phys.* **93** 10018–29

[26] Hung E S and Senturia S D 1999 Generating efficient dynamic models for micro- electromechanical systems from a few finite-element simulation runs *J. Microelectromech. Syst.* **9** 270–8

[27] Neilson G N and Barbastathis G 2006 Dynamic pull-in of parallel-plate and torsional electrostatic MEMS actuators *J. Microelectromech. Syst.* **15** 811–21

[28] Elata D and Bamberger H 2006 On the dynamic pull-in of electrostatic actuators with multiple degrees of freedom and multiple voltage sources *J. Microelectromech. Syst.* **15** 131–40

[29] Rhoads J F, Shaw S W and Turner K 2006 The nonlinear response of resonant microbeam systems with purely-parametric electrostatic actuation *J. Micromech. Microeng* **16** 890–9

[30] Li H, Preidikman S and Balachandran B 2005 Nonlinear forced oscillations of piezoelectric resonators *Proc. SPIE—The Int. Soc. Opt. Eng.* **5757** 30–41

[31] Wolf K and Gottlieb O 2002 Nonlinear dynamics of a noncontacting atomic force microscope cantilever actuated by a piezoelectric layer *J. Appl. Phys.* **91** 4701–9

[32] Rocha L A, Cretu E and Wolffenbuttal R F 2006 Using dynamic voltage drive in a parallel-plate electrostatic actuator for full-gap travel range positioning *J. Microelectromech. Syst.* **15** 69–83

[33] Sudipto K D and Aluru N R 2005 Complex oscillations and chaos in electrostatic microelectromechanical systems under superharmonic excitations *Phys. Rev. Lett.* **94** 204101

[34] Batra R C, Porfiri M and Spinello D 2008 Vibrations of narrow microbeams predeformed by an electric field *J. Sound Vib.* **309** 600–12

[35] Krylov S 2007 Lyapunov exponents as a criterion for the dynamic pull-in instability of electrostatically actuated microstructures *Int. J. Nonlinear Mech.* **42** 626–42

[36] Nayfeh A H, Younis M I and Abdel-Rahman E M 2005 Reduced-order models for MEMS applications *Nonlinear Dyn.* **41** 211–36

[37] Luo A C J and Wang F Y 2004 Nonlinear dynamics of a micro-electro-mechanical system with time-varying capacitors *ASME J. Vib. Acoust.* **126** 77–83

[38] Lenci S and Rega G 2006 Control of pull-in dynamics in a nonlinear thermoelastic electrically actuated microbeam *J. Micromech. Microeng* **16** 390–401

[39] Borovic B, Lewis F L, Liu A Q, Kolesar E S and Popa D 2006 The lateral instability problem in electrostatic comb drive actuators: modeling and feedback control *J. Micromech. Microeng.* **16** 1233–41

[40] Maithripala D H S, Berg J M and Dayawansa W P 2005 Control of an electrostatic microelectromechanical system using static and dynamic output feedback *ASME J. Dyn. Syst. Meas. Control* **127** 443–50

[41] Seeger J and Crary S 1997 Stabilization of electrostatically actuated mechanical devices *Proc. Int. Conf. Solid State Sens. And Actuators: TRANSDUCERS* vol 2 pp 1133–6

[42] Castaner J, Pons J, Nadal-Guardia R and Rodriguez 2001 Analysis of extended actuation range of electrostatic actuators by current pulse drive *Sensors Actuators* A **90** 181–90

[43] Osterberg P M and Senturia S D 1997 M-test: a test chip for MEMS material property measurement using electrostatically actuated test structures *J. Microelectromech. Syst.* **6** 107–18

[44] Senturia S D 2001 *Microsystems Design* (Dordrecht: Kluwer)

[45] Furlani E P 1999 Theory and simulation of viscous damped reflection phase gratings *J. Phys. D: Appl. Phys.* D **32** 412–6

[46] McCarthy B, Adams G G, McGruer N E and Potter D 2002 A dynamic model, including contact bounce, of an electrostatically actuated microswitch *J. Microelectromech. Syst.* **11** 276–83

[47] Bogdanov R I 1975 Versal deformations of a singular point on the plane in the case of zero eigenvalues *Funct. Anal. Appl.* **9** 144–5

[48] Takens F 1974 Singularities of vector fields *Publ. Math. IHES* **43** 47–100

[49] Carr J, Chow S N and Hale J K 1985 Abelian integrals and bifurcation theory *J. Diff. Eqns* **59** 413–36

[50] Intellisense Software Corporation 2005 Thermo-electro-mechanical module—device analysis and simulation *Intellisuite User Menual* Chapter 6